Supporting Information for "A coupled geochemical-geodynamical approach for predicting mantle melting in space and time"

P. W. Ball[1,2], T. Duvernay[2], and D. R. Davies[2]

[1]Department of Geosciences, Colorado State University, Fort Collins, CO 80523, USA.

[2]Research School of Earth Sciences, Australian National University, Canberra, ACT 2601, Australia.

Contents of this file

Introduction

Text S1 provides additional information on the implementation of melting in our geodynamic simulations. Text S2 describes how we calculate element partition coefficients as a function of pressure, temperature and composition. Text S3 describes how we estimate mineral major element compositions for calculating element partition coefficients. Text S4 describes an alternative method for calculating the melt-focusing distance (x_f).

Corresponding author: P. W. Ball, Department of Geosciences, Warner College of Natural Resources, Colorado State University, Fort Collins, CO 80523, USA. (patrick.ball@colostate.edu)

Text S1. Physical Melting Model

Melt fraction as a function of pressure and temperature, $X(P,T)$, is calculated using the equations of Katz, Spiegelmann, and Langmuir (2003). Entropy of fusion, thermal heat capacity, and expansivity of solid peridotite are updated to 407 J kg^{-1} K^{-1}, 1187 J kg^{-1} K^{-1}, and 3×10^{-5} K^{-1}, respectively, in line with additional experimental data (Shorttle et al., 2014). The Katz et al. (2003) melting model contains a number of coefficients which must be parameterized by fitting to peridotite melting experiments. Since we require the mineralogy of the residue to be recorded during these experiments, this physical melting model is constrained using a greater variety of experimental data than we have used to parameterize our geochemical melting model. Therefore, we have chosen to update a number of these constants to increase consistency between the melting model and our restricted database. The melt fraction at which clinopyroxene is exhausted, $X_{cpx-out}$, is a function of the weight fraction of clinopyroxene in the solid peridotite, M_{cpx}, and the reaction coefficient, R_{cpx}, which is a function of pressure, P,

$$\text{i.e., } X_{cpx-out} = \frac{M_{cpx}}{R_{cpx}(P)}, \tag{1}$$

$$\text{where } R_{cpx} = R_1 + R_2 P. \tag{2}$$

Our geochemical melting model is constrained using experiments conducted on MM3 and KR4003 peridotites (Baker & Stolper, 1994; Walter, 1998; Falloon et al., 1999). $X_{cpx-out}$ is predicted to decrease as a function of pressure within the Katz et al. (2003) melting parameterization. However, in these experiments, $X_{cpx-out}$ increases as a function of pressure (Figure S1). Here, we exploit the M_{cpx} and $X_{cpx-out}$ values recorded within these experiments to approximate M_{cpx}, R_1 and R_2 as 0.18, 0.94 and -0.1, respectively. To

provide a good fit for melt fraction as a function of temperature, two additional constants, β_2 and B_1, are also updated to 1.2 and 1520 °C, respectively (Figure S2).

The decompression melting model parameterised by Katz et al. (2003) assumes that no heat is lost during melting. However, it is necessary to modify these equations in this case since within our geodynamic model we allow heat diffusion to occur. We replace the adiabatic gradient term with the actual temperature gradient that is experienced by each particle in the geodynamic model using Equations 3–5 in the main text. This replacement requires the following thermodynamic assumption:

$$\frac{\alpha}{\rho} = -\frac{dS}{dP}\bigg|_T = \frac{dS}{dT}\bigg|_P \frac{dT}{dP}\bigg|_S \sim \frac{C_P}{T}\frac{dT}{dP}\bigg|^{Fluidity}, \tag{3}$$

where P, T and S are pressure, temperature and entropy, respectively; and α, ρ and C_P denote thermal expansivity, density and heat capacity, respectively.

The lherzolite melting parameterization of Katz et al. (2003) is a hydrous parameterization and so a weight fraction of water present within the source region (F_{H_2O}) must be estimated. F_{H_2O} in primitive mantle is assumed to be 280 ppm and is approximated from the concentration of Ce within the source region (F_{Ce}) by assuming that $F_{H_2O}/F_{Ce} = 200$ (Michael, 1995). F_{H_2O} in depleted mantle is taken to be 100 ppm (Salters & Stracke, 2004).

Text S2. Distribution Coefficients

To calculate the bulk distribution coefficient for a given element within the solid assemblage, $\bar{D}$, the partition coefficients for each mineral, D_{min}, must be parameterized. Our model includes two options for how D_{ol}, D_{opx}, D_{cpx} and D_{gar} are calculated. Partition

coefficients can either be assumed to be constant using the values listed in Table S1, or they can vary as a function of pressure (P), temperature (T) and mineral chemistry. D_{spl} is assumed to be constant as a function of P and X for all elements. In the mantle, partition coefficients necessarily vary as a function of P, T and mineral chemistry as sites within mineral lattices expand and contract. The partitioning of an element with a charge $v+$ and a radius r_i entering into site M of a crystalline lattice is governed by the lattice strain equation,

$$D_i = D^{v+}_{0(M)} \times \exp\left[\frac{-4\pi N_A E^{v+}_M}{RT}\left(\frac{1}{2}r^{v+}_{0(M)}\left(r_i - r^{v+}_{0(M)}\right)^2 + \frac{1}{3}\left(r_i - r^{v+}_{0(M)}\right)^3\right)\right], \quad (4)$$

where N_A is Avogadro's number, R is the gas constant, E^{v+}_M is the Young's modulus of lattice site M, $r^{v+}_{0(M)}$ is the radius of the site and $D^{v+}_{0(M)}$ is the partition coefficient for an element with a charge $v+$ and a radius $r^{v+}_{i(M)}$ (Brice, 1975; Wood & Blundy, 1997). $v+$ and r_i for each element are listed in Table S1. Elemental radii are dependent upon the stoichiometry of the mineral site that the element is entering. For olivine, each element is in a six-fold coordination, r_i (VI), for pyroxene and garnet each element is in an eight-fold coordination, r_i (VIII). Note that any element where ionic radii in six- or eight-fold coordination is not recorded is assigned a constant partition coefficient for minerals that require those variables to calculate partition coefficients (McKenzie & O'Nions, 1995).

Olivine

For Olivine, $D^{v+}_{0(M)}$, E^{v+}_M and $r^{v+}_{0(M)}$ are calculated for 3+ valency cations, such as the REEs and Y, using the equations of Sun and Liang (2013),

$$D^{3+}_{0(ol)} = \exp\left(-0.45 - 0.11P + 1.54\chi^{\mathrm{Al}}_{\mathrm{Mel}} - 1.94\mathrm{Mg\#}\right), \quad (5)$$

$$E^{3+}_{ol} = 426 \times 10^9, \quad (6)$$

$$r^{3+}_{0(ol)} = 0.72 \times 10^{-10}. \tag{7}$$

Where χ^{Al}_{min} is the modal proportion of Al in a mineral, which in this case is olivine (ol), and can be calculated by

$$\chi_i = i_{mol} \times C_i \times \frac{1}{O_{min}} \sum_{i}^{I} i_{mol} O_i, \tag{8}$$

$$\mathrm{Mg\#} = \frac{F^{\mathrm{Mg}}_{min}}{F^{\mathrm{Mg}_{min}} + F^{\mathrm{Fe}}_{min}}, \tag{9}$$

where χ_i, i_{mol}, C_i, O_i and O_{min} are the proportions of oxide i within the mineral, fraction by weight of oxide i within the mineral divided by its molecular weight, the number of cations in the oxide i, the number of oxygen atoms in the oxide i and the number of oxygen atoms in the mineral, respectively. O_{ol}, O_{opx}, O_{cpx} and O_{gnt} are 4, 6, 6 and 12, respectively. All other constants are listed in Table S2.

The partition coefficients between olivine and melt for elements with 1+, 2+, 4+ or 5+ valency are assigned using a compilation of constant values (McKenzie & O'Nions, 1995).

Orthopyroxene

The partition coefficients for +3 valency cations partitioning into orthopyroxene are calculated using the parameterization of Yao, Sun, and Liang (2012),

$$D^{3+}_{0(opx)} = \exp\left(-5.37 + \frac{38700}{RT} + 3.54\chi^{T}_{\mathrm{Al}} + 3.56\chi^{M2}_{\mathrm{Ca}}\right), \tag{10}$$

$$E^{3+}_{opx} = \left(-1.37 + 1.85 r_0 - 0.53\chi^{M2}_{\mathrm{Ca}}\right) \times 10^{12}, \tag{11}$$

$$\text{where } r^{3+}_{0(opx)} = \left(0.69 + 0.23\chi^{M2}_{\mathrm{Mg}} + 0.43 F^{M2}_{\mathrm{Ca}}\right) \times 10^{-10}. \tag{12}$$

Within pyroxenes, the amount of Ca, Mg and Al entering either the $M1$, $M2$ or tetrahedral site are calculated assuming all Ca, Na, K and Mn are assigned to the $M2$ site, all Ti and Cr are assigned to the $M1$ site, and that Fe and Mg are equally distributed across

$M1$ and $M2$ (Wood & Banno, 1973). Finally, any Al that cannot fit in the $M1$ site is assigned to the tetrahedral site so that,

$$\chi^{M2}_{\mathrm{Mg}} = (1 - \chi_{\mathrm{Ca}} - \chi_{\mathrm{Na}} - \chi_{\mathrm{K}} - \chi_{\mathrm{Mn}}) \times \mathrm{Mg\#}, \tag{13}$$

$$\chi^{M2}_{\mathrm{Ca}} = \chi_{\mathrm{Ca}}, \tag{14}$$

$$\chi^{M1}_{\mathrm{Al}} = 1 - \chi_{\mathrm{Ti}} - \chi_{\mathrm{Cr}} - \left(\chi_{\mathrm{Mg}} + \chi_{\mathrm{Fe}} - \frac{\chi^{M2}_{\mathrm{Mg}}}{\mathrm{Mg\#}} \right), \tag{15}$$

$$\chi^{T}_{\mathrm{Al}} = \chi_{\mathrm{Al}} - \chi^{M1}_{\mathrm{Al}}. \tag{16}$$

The constants within the lattice-strain model for +2 cations ($D^{2+}_{0(opx)}$, E^{2+}_{opx} and $r^{2+}_{0(opx)}$) are parameterized from the constants for 3+ cations and relative to Mg (Hazen & Finger, 1979; Wood & Blundy, 2014),

$$E^{2+}_{opx} = \frac{2}{3} E^{3+}_{opx}, \tag{17}$$

$$r^{2+}_{0(opx)} = r^{3+}_{0(opx)} + 0.08 \times 10^{-10}, \tag{18}$$

$$r_{Mg} = 0.89 \times 10^{-10}, \tag{19}$$

$$D^{2+}_{i} = \exp\left[\frac{-4\pi N_A E^{2+}_{opx}}{RT} \left(\frac{r^{2+}_{0}}{2} (r^2_{\mathrm{Mg}} - r^2_i) + \frac{1}{3} (r^3_i - r^3_{\mathrm{Mg}}) \right) \right]. \tag{20}$$

For 1+, 4+ and 5+ valency cations, partition coefficients between orthopyroxene and melt are assigned constant values from a compilation of experimental results (McKenzie & O'Nions, 1995).

Clinopyroxene

The partition coefficients between clinopyroxene and melt for 3+ cations are set using the parameterization of Sun and Liang (2012),

$$D^{3+}_{0(cpx)} = \exp\left(-7.14 + \frac{7.19 \times 10^4}{RT} + 4.37 \chi^{M1}_{\mathrm{Al}} + 1.98 \chi^{M2}_{\mathrm{Mg}} - 0.91 \chi_{\mathrm{H_2O}} \right), \tag{21}$$

$$E^{3+}_{cpx} = \left(2270 r^{3+}_{0(cpx)} - 2000 \right) \times 10^9, \tag{22}$$

where $r^{3+}_{0(cpx)} = \left(1.066 - 0.104\chi^{M1}_{\mathrm{Al}} - 0.212\chi^{M2}_{\mathrm{Mg}}\right) \times 10^{-10}$. (23)

The constants within the lattice-strain model for +1 cations ($D^{1+}_{0(cpx)}$, E^{1+}_{cpx} and $r^{1+}_{0(cpx)}$) are parameterized from the constants for 3+ cations and relative to D^{1+}_{Na} (Hazen & Finger, 1979; Blundy et al., 1995; Wood & Blundy, 2014),

$$D^{\mathrm{Na}}_0 = \exp\left(\frac{10367 + 2100P - 165P^2}{T} - 10.27 + 0.358P - 0.0184P^2\right), \quad (24)$$

$$r_{\mathrm{Na}} = 1.18 \times 10^{-10}, \quad (25)$$

$$r^{1+}_0 = r^{3+}_0 + 0.12 \times 10^{-10}, \quad (26)$$

$$E^{1+}_{cpx} = \frac{1}{3}E^{3+}_{cpx}, \quad (27)$$

$$D^{1+}_i = D^{\mathrm{Na}}_0 \exp\left[\frac{-4\pi N_A E^{1+}_{cpx}}{RT}\left(\frac{r^{1+}_0}{2}\left(r^2_{\mathrm{Na}} - r^2_i\right) + \frac{1}{3}\left(r^3_i - r^3_{\mathrm{Na}}\right)\right)\right]. \quad (28)$$

Constants within the lattice-strain model for +2 cations are parameterized from the constants for 3+ cations and relative to D^{2+}_{Ca}

$$D^{Ca}_{0(cpx)} = 2, \quad (29)$$

$$r_{\mathrm{Ca}} = 1.12 \times 10^{-10}, \quad (30)$$

$$E^{2+}_{cpx} = \frac{2}{3}E^{3+}_{cpx}, \quad (31)$$

$$r^{2+}_{0(cpx)} = r^{3+}_{0(cpx)} + 0.06 \times 10^{-10}, \quad (32)$$

$$D^{2+}_i = D^{\mathrm{Ca}}_0 \exp\left[\frac{-4\pi N_A E^{2+}_{cpx}}{RT}\left(\frac{r^{1+}_0}{2}\left(r^2_{\mathrm{Ca}} - r^2_i\right) + \frac{1}{3}\left(r^3_i - r^3_{\mathrm{Ca}}\right)\right)\right] \quad (33)$$

(Hazen & Finger, 1979; Blundy & Wood, 2003; Hill et al., 2011; Wood & Blundy, 2014). Constants within the lattice-strain model for +4 cations are parameterized from the constants for 3+ cations and relative to D^{4+}_{Th} (Hazen & Finger, 1979; Landwehr et al., 2001; Wood & Blundy, 2014),

$$D^{\mathrm{Th}}_{0(cpx)} = \exp\left(\frac{214790 - 175.7T + 16420P - 1500P^2}{RT}\right)\frac{\chi^{\mathrm{Mel}}_{\mathrm{Mg}}}{\chi^{M1}_{\mathrm{Mg}}Y^{M1}_{\mathrm{Mg}}Y^{M2}_{\mathrm{Th}}}, \quad (34)$$

$$E_{cpx}^{4+} = \frac{4}{3} E_{cpx}^{3+}, \tag{35}$$

$$r_{0(cpx)}^{4+} = r_{0(cpx)}^{3+}, \tag{36}$$

$$r_{\mathrm{Th}} = 1.041 \times 10^{-10}, \tag{37}$$

$$D_i^{4+} = D_{0(cpx)}^{\mathrm{Th}} \exp\left[\frac{-4\pi N_A E_{cpx}^{4+}}{RT}\left(\frac{r_0^{4+}}{2}\left(r_{\mathrm{Th}}^2 - r_i^2\right) + \frac{1}{3}\left(r_i^3 - r_{\mathrm{Th}}^3\right)\right)\right], \tag{38}$$

$$\text{where } Y_{\mathrm{Mg}}^{M1} = \exp\left[\frac{902\left(1 - \chi_{\mathrm{Mg}}^{M1}\right)^2}{T}\right], \tag{39}$$

$$\text{and } Y_{\mathrm{Th}}^{M2} = \exp\left[\frac{4\pi N_A E_{cpx}^{4+}}{RT}\left(\frac{r_0^{4+}}{2}\left(r_{\mathrm{Th}} - r_0^{4+}\right)^2 + \frac{1}{3}\left(r_{\mathrm{Th}} - r_0^{4+}\right)^3\right)\right]. \tag{40}$$

A constant partition coefficient between melt and clinopyroxene is used for elements with 5+ valency (McKenzie & O'Nions, 1995).

Garnet

The partition coefficients between garnet and melt for elements with 3+ valency are parameterized using the equations of Sun and Liang (2013),

$$D_{0(gar)}^{3+} = \exp\left(-2.05 + \frac{91700 - 3471.3P + 91.35P^2}{RT} - 1.02\chi_{\mathrm{Ca}}\right), \tag{41}$$

$$E_{gar}^{3+} = \left(-1620 + 2290 r_{0(gar)}^{3+}\right) \times 10^9, \tag{42}$$

$$\text{where } r_{0(gar)}^{3+} = (0.78 + 0.155\chi_{\mathrm{Ca}}) \times 10^{-10}. \tag{43}$$

The constants within the lattice-strain model for elements with +2 valency are parameterized from the constants for elements with 3+ valency and relative to D_{Mg}^{2+} (Hazen & Finger, 1979; Wood & Blundy, 2014),

$$E_{gar}^{2+} = \frac{2}{3} E_{gar}^{3+}, \tag{44}$$

$$r_{0(gar)}^{2+} = r_{0(gar)}^{3+} + 0.053 \times 10^{-10}, \tag{45}$$

$$r_{\mathrm{Mg}} = 0.89 \times 10^{-10}, \tag{46}$$

$$D_{\mathrm{Mg}} = \frac{\exp\left(\dfrac{258210 - 141.5T + 5418P}{3RT}\right)}{\exp\left(\dfrac{19000\chi^2_{\mathrm{Ca}}}{RT}\right)}, \tag{47}$$

$$D_i^{2+} = D_{\mathrm{Mg}}\exp\left[\frac{-4\pi N_A E^{2+}_{gar}}{RT}\left(\frac{r_0}{2}\left(r^2_{\mathrm{Mg}} - r_i^2\right) + \frac{1}{3}\left(r_i^3 - r^3_{\mathrm{Mg}}\right)\right)\right]. \tag{48}$$

The constants within the lattice-strain model to calculate partition coefficients between garnet and melt for elements with +4 valency are parameterized using the values of Mallmann and O'Neill (2007),

$$D^{4+}_{0(gar)} = 4.38, \tag{49}$$

$$E^{4+}_{gar} = 2753 \times 10^9, \tag{50}$$

$$r^{v+}_{0(M)} = 0.6626 \times 10^{-10}. \tag{51}$$

Partition coefficients for elements with 1+ or 5+ valency are parameterized as fixed values (McKenzie & O'Nions, 1995).

Spinel

Partition coefficients between spinel and melt for all elements are assumed to be constant values (McKenzie & O'Nions, 1995).

Text S3. Peridotite Model Description

Mineral Compositions

Mineral compositions are required to calculate bulk partition coefficients (Sun & Liang, 2012; Yao et al., 2012; Sun & Liang, 2013). The same experimental database outlined in Section 2 of the main text is used to parameterize mineral compositions as a function of pressure and/or melt fraction (Baker & Stolper, 1994; Falloon et al., 1999; Walter, 1998).

Olivine

Figure S3 shows χ_{Al} and Mg# in olivine as a function of melt fraction. The presence of garnet as a stable phase significantly alters the compositions of other minerals so that parameterizations for spinel- and garnet-bearing peridotites must be calibrated individually. χ_{Al} does not vary with pressure or melt fraction and is fixed as 0.00156 and 0.00564 in spinel- and garnet-bearing peridotites, respectively (Figures S3a,b). Mg# increases as melt fraction (X) increases by

$$\mathrm{Mg\#} = 0.059X + 0.904 \text{ and } \mathrm{Mg\#} = 0.070X + 0.897 \tag{52}$$

for spinel- and garnet- peridotite, respectively (Figures S3c,d).

Orthopyroxene

Orthopyroxene compositions vary differently with melt fraction depending on whether clinopyroxene is a stable phase. When clinopyroxene is stable, χ^{M2}_{Mg} decreases and χ^{M2}_{Ca} increases as melt fraction increases. These trends reverse when clinopyroxene is exhausted (Figure S4). There is no significant difference in orthopyroxene composition as a function of pressure or aluminous phase. Therefore we fit χ^{M2}_{Mg}, χ^{T}_{Al} and χ^{M2}_{Ca} in orthopyroxene using a second order polynomial on all available data,

$$\chi^{M2}_{\mathrm{Mg}} = 0.692X^2 - 0.176X + 0.834, \tag{53}$$

$$\chi^{T}_{\mathrm{Al}} = -0.675X^2 + 0.041X + 0.146, \tag{54}$$

$$\chi^{M2}_{\mathrm{Ca}} = -0.756X^2 + 0.273X + 0.063. \tag{55}$$

Clinopyroxene

χ^{M2}_{Mg}, χ^{T}_{Al}, and χ^{M1}_{Al} in clinopyroxene vary linearly as a function of melt fraction but depend significantly on whether garnet is a stable phase (Figure S5). If spinel is stable,

$$\chi^{M2}_{\mathrm{Mg}} = 0.583X + 0.223,\ \chi^{T}_{\mathrm{Al}} = -0.177X + 0.154, \text{ and } \chi^{M1}_{\mathrm{Al}} = -0.438X + 0.137, \quad (56)$$

and if garnet is stable,

$$\chi^{M2}_{\mathrm{Mg}} = 0.422X + 0.547,\ \chi^{T}_{\mathrm{Al}} = -0.013X + 0.061, \text{ and } \chi^{M1}_{\mathrm{Al}} = -0.114X + 0.099. \quad (57)$$

To calculate partition coefficients between clinopyroxene and melt for elements with +4 valency requires a parameterization for χ^{M1}_{Mg} and χ^{Mel}_{Mg}. Both χ^{M1}_{Mg} and χ^{Mel}_{Mg} vary linearly as a function of X and strongly depend on whether spinel- or garnet-bearing peridotite is melting (Figure S5). If spinel is stable, χ^{M1}_{Mg} and χ^{Mel}_{Mg} can be parameterized as

$$\chi^{M1}_{\mathrm{Mg}} = 0.425X + 0.741 \text{ and } \chi^{Mel}_{\mathrm{Mg}} = 0.140X + 0.722, \quad (58)$$

whereas if garnet is stable,

$$\chi^{M1}_{\mathrm{Mg}} = 0.191X + 0.793 \text{ and } \chi^{Mel}_{\mathrm{Mg}} = 0.207X + 0.701. \quad (59)$$

Garnet

Finally, χ_{Ca} in garnet decreases as a function of melt fraction,

$$\chi_{\mathrm{Ca}} = -0.247X + 0.355. \quad (60)$$

Text S4. Calculating x_f Using Extraction Efficiency

Extraction efficiency is defined as the ratio of the volume of melt erupted over the total volume of melt produced (Keller et al., 2017). To calculate the expected extraction

efficiency within our simulations based on the extraction efficiency results of Keller et al. (2017) we must correct for three factors. First, their simulations of varying T_p have a constant R_s of 3 cm yr^{-1}, whereas our models have an R_s of 2.1 cm yr^{-1}. Second, their simulations of varying R_s have a constant T_p of 1350 °C, while ours have a T_p of 1325 °C. Third, to provide a better fit to crustal thickness observations, Keller et al. (2017) reduce their MORB proportion from 25% to 19% and so the results published in Figure 4 of their paper cannot be used directly. Therefore, we apply the following approach. First, we calculate regressions through their extraction efficiency results as a function of R_s, T_p and MORB proportion for a bulk mantle source (open squares in Figures 4f, 4h and 4i of Keller et al., 2017). Then, for each parameter, we compute the difference in extraction efficiency between their reference value and ours (e.g., the difference between extraction efficiency at $R_s = 3$ cm yr^{-1} and 2.1 cm yr^{-1}). Finally, using linear combinations of the obtained differences (e.g. differences in MORB content and half-spreading rate for data at variable potential temperature), we adjust Keller et al. (2017) extraction efficiency results and calculate new regressions applicable to our simulations.

In this context, we define x_f as the lateral distance from the ridge axis encompassing a volume of melt equal to the extraction efficiency times the total amount of melt produced within the whole melting region. In doing so, we assume full melt extraction at distances $< x_f$ and exclude any contribution from melts generated farther away. For each of our simulations, we use the previously obtained regressions to compute the extraction efficiency and deduce x_f accordingly.

References

Baker, M. B., & Stolper, E. M. (1994). Determining the composition of high-pressure mantle melts using diamond aggregates. *Geochimica et Cosmochimica Acta*, *58*(13), 2811–2827.

Blundy, J., Falloon, T., Wood, B., & Dalton, J. (1995). Sodium partitioning between clinopyroxene and silicate melts. *Journal of Geophysical Research: Solid Earth*, *100*(B8), 15501–15515.

Blundy, J., & Wood, B. (2003). Partitioning of trace elements between crystals and melts. *Earth and Planetary Science Letters*, *210*(3-4), 383–397.

Brice, J. (1975). Some thermodynamic aspects of the growth of strained crystals. *Journal of Crystal Growth*, *28*(2), 249–253.

Falloon, T. J., Green, D. H., Danyushevsky, L. V., & Faul, U. H. (1999). Peridotite melting at 1.0 and 1.5 GPa: an experimental evaluation of techniques using diamond aggregates and mineral mixes for determination of near-solidus melts. *Journal of Petrology*, *40*(9), 1343–1375.

Hazen, R. M., & Finger, L. W. (1979). Bulk modulus—volume relationship for cation-anion polyhedra. *Journal of Geophysical Research: Solid Earth*, *84*(B12), 6723–6728.

Hill, E., Blundy, J. D., & Wood, B. J. (2011). Clinopyroxene–melt trace element partitioning and the development of a predictive model for HFSE and Sc. *Contributions to Mineralogy and Petrology*, *161*(3), 423–438.

Katz, R. F., Spiegelmann, M., & Langmuir, C. H. (2003). A new parameterization of hydrous mantle melting. *Geochemistry, Geophysics, Geosystems*, *4*(9). doi: 10.1029/2002GC000433

Keller, T., Katz, R. F., & Hirschmann, M. M. (2017). Volatiles beneath mid-ocean ridges: Deep melting, channelised transport, focusing, and metasomatism. *Earth and Planetary Science Letters*, *464*, 55–68.

Landwehr, D., Blundy, J., Chamorro-Perez, E. M., Hill, E., & Wood, B. (2001). U-series disequilibria generated by partial melting of spinel lherzolite. *Earth and Planetary Science Letters*, *188*(3-4), 329–348.

Mallmann, G., & O'Neill, H. S. C. (2007). The effect of oxygen fugacity on the partitioning of Re between crystals and silicate melt during mantle melting. *Geochimica et Cosmochimica Acta*, *71*(11), 2837–2857.

McDonough, W. F., & Sun, S. S. (1995). The composition of the Earth. *Chemical Geology*, *120*(3-4), 223–253. doi: 10.1016/0009-2541(94)00140-4

McKenzie, D., & O'Nions, R. K. (1995). The Source Regions of Ocean Island Basalts. *Journal of Petrology*, *36*(1), 133–159.

Michael, P. (1995). Regionally distinctive sources of depleted MORB: Evidence from trace elements and H_2O. *Earth and Planetary Science Letters*, *131*(3–4), 301–320. doi: 10.1016/0012-821X(95)00023-6

Salters, V. J. M., & Stracke, A. (2004). Composition of the depleted mantle. *Geochemistry, Geophysics, Geosystems*, *5*(5). doi: 10.1029/2003GC000597

Shannon, R. D. (1976). Revised effective ionic radii and systematic studies of interatomic distances in halides and chalcogenides. *Acta crystallographica section A: crystal physics, diffraction, theoretical and general crystallography*, *32*(5), 751–767.

Shorttle, O., Maclennan, J., & Lambart, S. (2014). Quantifying lithological variability in the mantle. *Earth and Planetary Science Letters*, *395*, 24–40.

Sun, C., & Liang, Y. (2012). Distribution of REE between clinopyroxene and basaltic melt along a mantle adiabat: effects of major element composition, water, and temperature. *Contributions to Mineralogy and Petrology*, *163*(5), 807–823.

Sun, C., & Liang, Y. (2013). The importance of crystal chemistry on REE partitioning between mantle minerals (garnet, clinopyroxene, orthopyroxene, and olivine) and basaltic melts. *Chemical Geology*, *358*, 23–36.

Walter, M. J. (1998). Melting of garnet peridotite and the origin of komatiite and depleted lithosphere. *Journal of Petrology*, *39*(1), 29–60. doi: 10.1093/petrology/39.1.29

Wood, B. J., & Banno, S. (1973). Garnet-orthopyroxene and orthopyroxene-clinopyroxene relationships in simple and complex systems. *Contributions to Mineralogy and Petrology*, *42*(2), 109–124.

Wood, B. J., & Blundy, J. D. (1997). A predictive model for rare earth element partitioning between clinopyroxene and anhydrous silicate melt. *Contributions to Mineralogy and Petrology*, *129*(2-3), 166–181.

Wood, B. J., & Blundy, J. D. (2014). Trace element partitioning: the influences of ionic radius, cation charge, pressure, and temperature. In H. D. Holland & K. K. Turekian (Eds.), *Treatise on geochemistry* (Vol. 3, pp. 421–448). Elsevier.

Yao, L., Sun, C., & Liang, Y. (2012). A parameterized model for REE distribution between low-Ca pyroxene and basaltic melts with applications to REE partitioning in low-Ca pyroxene along a mantle adiabat and during pyroxenite-derived melt and peridotite interaction. *Contributions to Mineralogy and Petrology*, *164*(2), 261–280.

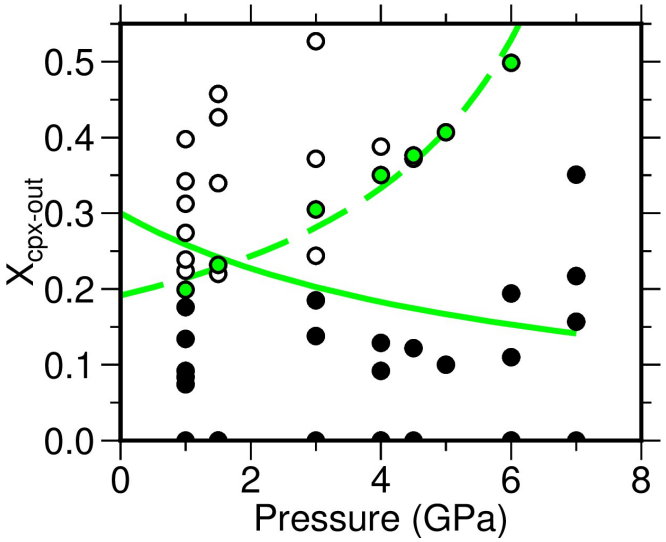

Figure S1. Comparison between anhydrous melting model parameterisation predictions of the melt fraction at which clinopyroxene is exhausted ($X_{cpx-out}$) as a function of pressure. Closed/open circles = peridotite melting experiments where clinopyroxene is present/absent in the residue (Baker & Stolper, 1994; Walter, 1998; Falloon et al., 1999). Green circles = $X_{cpx-out}(P)$ constrained by fitting to experimental data, note that experiments conducted at 3 and 5 GPa were not used to predict modal mineralogy (see Section 3.2 of main text). Solid/dashed line = original/updated melting parameterization (Katz et al., 2003).

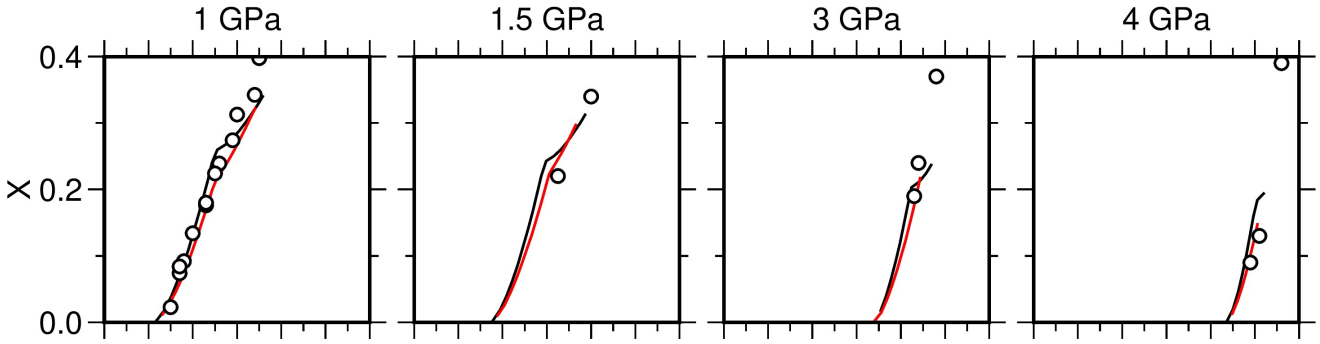

Figure S2. Comparison between experimental data and anhydrous melting model parameterisations at different pressures. Open circles = experimental results used to constrain our geochemical melting model (Baker & Stolper, 1994; Walter, 1998; Falloon et al., 1999). Black/red line = original/updated melting parameterization (Katz et al., 2003). Melting models are calculated from to T_p = 1100–1650 °C

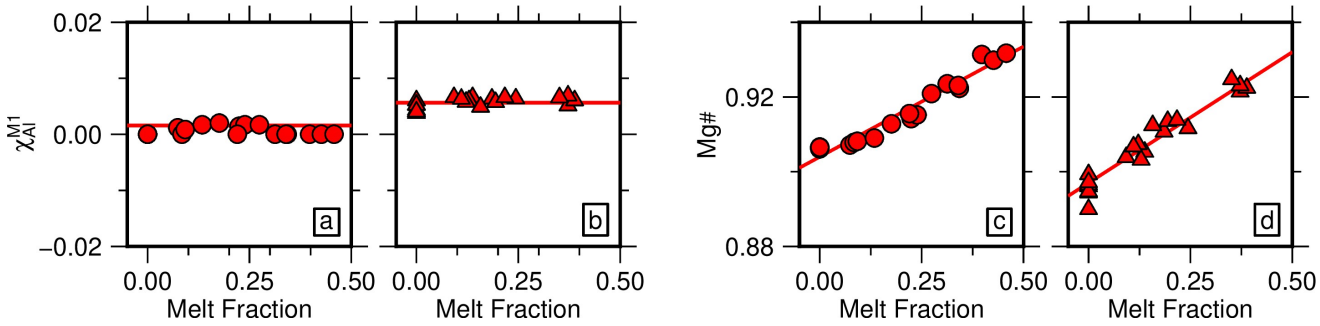

Figure S3. Olivine composition as a function of melt fraction, red circles/triangles = spinel/garnet peridotite melting experiments. Red lines = best-fit parameterisation described by Equation 52. a) $\chi_{\mathrm{Al}}^{\mathrm{M1}}$ as function of X for spinel peridotite. b) Same for garnet peridotite. c) Mg# as function of X for spinel peridotite. d) Same for garnet peridotite.

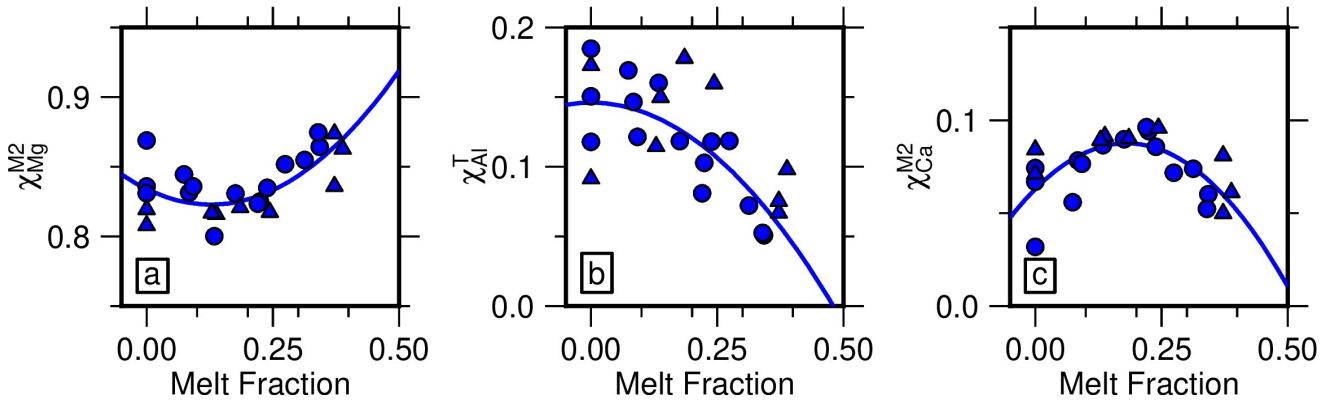

Figure S4. Orthopyroxene composition as a function of melt fraction, blue circles/triangles = spinel/garnet peridotite melting experiments. Blue lines = best-fit regression lines. a) $\chi^{\mathrm{M2}}_{\mathrm{Mg}}$ as a function of X, regression described by Equation 53. b) $\chi^{\mathrm{T}}_{\mathrm{Al}}$ as a function of X, regression described by Equation 54. c) $\chi^{\mathrm{M2}}_{\mathrm{Ca}}$ as a function of X, regression described by Equation 55.

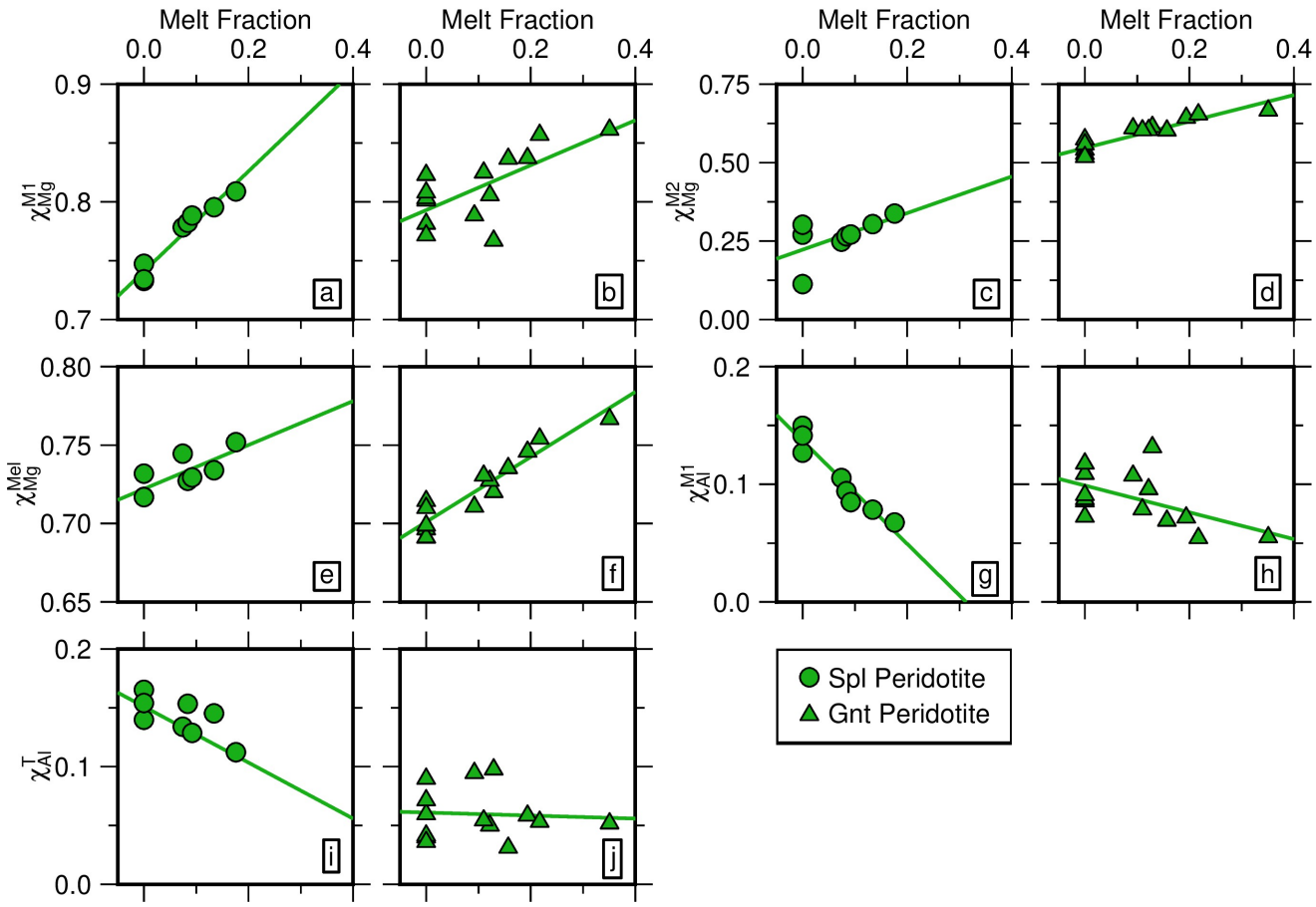

Figure S5. Clinopyroxene composition as a function of melt fraction, green circles/triangles = spinel/garnet peridotite melting experiments. Green lines = best-fit linear regressions for each set of compositions. a/b) $\chi^{\mathrm{M1}}_{\mathrm{Mg}}$ as function of X, regression described in Equation 56/57. c/d) same for $\chi^{\mathrm{M2}}_{\mathrm{Mg}}$. e/f) same for $\chi^{\mathrm{Mel}}_{\mathrm{Mg}}$. g/h) same for $\chi^{\mathrm{M1}}_{\mathrm{Al}}$. i/j) same for $\chi^{\mathrm{T}}_{\mathrm{Al}}$.

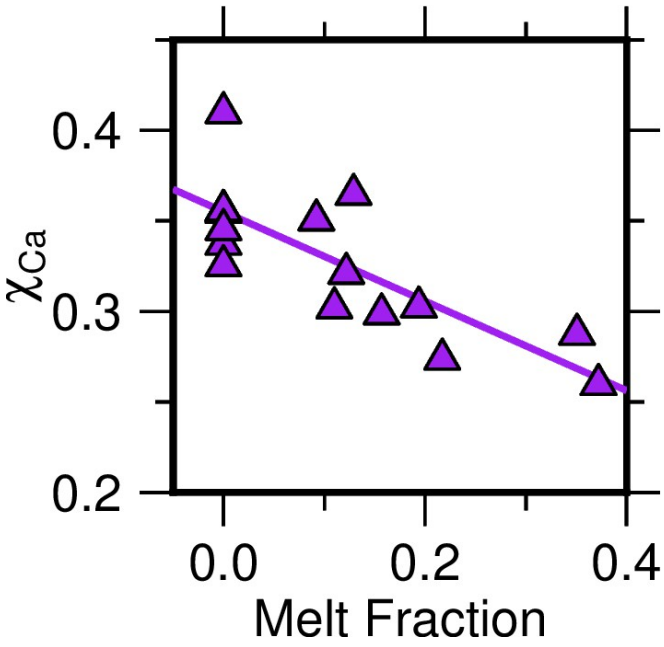

Figure S6. χ_{Ca} in garnet as a function of melt fraction, purple triangles = garnet peridotite melting experiments. Purple line = best-fit regression described by Equation 60.

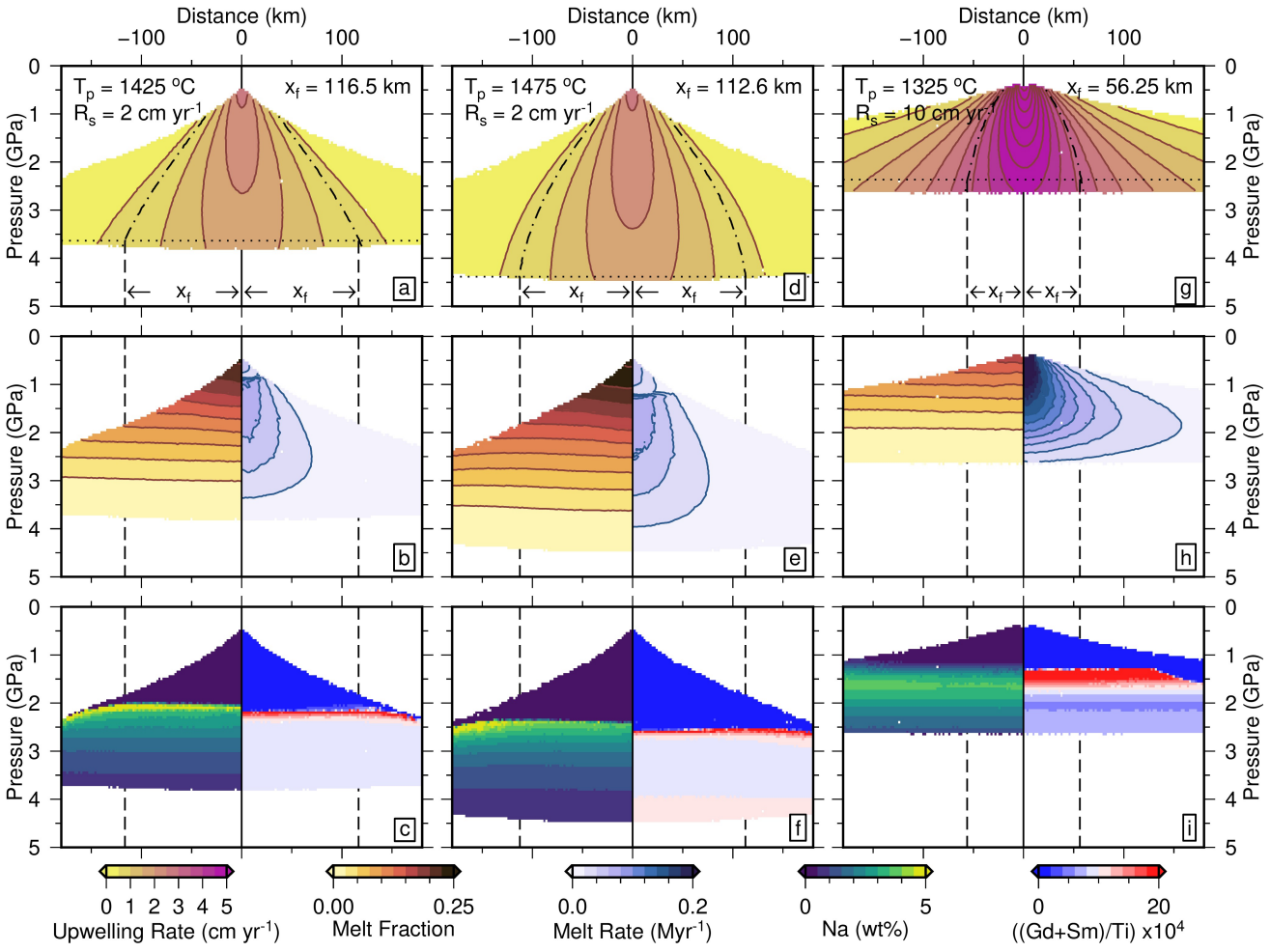

Figure S7. Melt region geometry at mid-oceanic ridges as a function of T_p and R_s. a) Ridge-centred model coloured by upwelling rate. Coloured region indicates where $X > 0$. Model run with T_p and R_s as indicated top-left; corresponding x_f for each model shown top right. b) Same as panel a but with left- and right-hand sides coloured by melt fraction and melting rate, respectively. c) Same as panel a but with left- and right-hand sides coloured by Na wt% and ((Gd+Sm)/Ti)x10^4 within the instantaneous melt phase, respectively. d–f) Same as panels a–c but with different T_p and R_s as indicated in top left corner of panel d. g-i) Same as panels d-f.

Table S1. Elemental compositions in primitive (Prim) and depleted (Dep) mantle, radii, valency and partition coefficients (Shannon, 1976; McDonough & Sun, 1995; McKenzie & O'Nions, 1995; Salters & Stracke, 2004)

Element	La	Ce	Pr	Nd	Sm	Eu	Gd	Tb	Dy	Ho	Er	Tm	Yb
Prim c_s (ppm)	0.648	1.675	0.254	1.25	0.406	0.154	0.544	0.099	0.674	0.149	0.438	0.068	0.441
Dep c_s (ppm)	0.234	0.772	0.131	0.713	0.27	0.107	0.395	0.075	0.531	0.122	0.371	0.06	0.401
r_i (VIII) (Å)	1.160	1.143	1.126	1.109	1.079	1.066	1.053	1.040	1.027	1.015	1.004	0.994	0.985
r_i (VI) (Å)	1.032	1.01	0.99	0.983	0.958	0.947	0.938	0.923	0.912	0.901	0.89	0.88	0.868
$v+$	3	3	3	3	3	3	3	3	3	3	3	3	3
D_{ol}	0.0004	0.0005	0.0008	0.001	0.0013	0.0016	0.0015	0.0015	0.0017	0.0016	0.0015	0.0015	0.0015
D_{cpx}	0.054	0.098	0.15	0.21	0.26	0.31	0.3	0.31	0.33	0.31	0.3	0.29	0.28
D_{opx}	0.002	0.003	0.0048	0.0068	0.01	0.013	0.016	0.019	0.022	0.026	0.03	0.04	0.049
D_{spl}	0.01	0.01	0.01	0.01	0.01	0.01	0.01	0.01	0.01	0.01	0.01	0.01	0.01
D_{gnt}	0.01	0.021	0.054	0.087	0.217	0.32	0.498	0.75	1.06	1.53	2.00	3.00	4.03

Element	Lu	Cs	Rb	K	Ba	Th	Pb	U	Nb	Sr	Zr	Hf	Ti
Prim c_s (ppm)	0.0675	0.021	0.6	240	6.6	0.0795	0.15	0.0203	0.658	19.9	10.5	0.283	1205
Dep c_s (ppm)	0.063	0.00132	0.088	60	1.2	0.0137	0.0232	0.0047	0.21	9.8	7.94	0.199	798
r_i (VIII) (Å)	0.977	1.74	1.61	1.51	1.42	1.041	0.94	0.983	0.74	1.26	0.84	0.83	0.74
r_i (VI) (Å)	0.861	1.67	1.52	1.38	1.35	0.94	0.775	0.89	0.64	1.18	0.72	0.71	0.605
$v+$	3	1	1	1	2	4	4	4	5	2	4	4	4
D_{ol}	0.0015	0.00005	0.00018	0.00018	0.0003	0.0001	0.0001	0.0001	0.005	0.00019	0.01	0.01	0.02
D_{cpx}	0.28	0.0002	0.001	0.002	0.0005	0.00026	0.01	0.00036	0.02	0.13	0.1	0.22	0.18
D_{opx}	0.060	0.0001	0.0006	0.001	0.0001	0.0001	0.0013	0.0001	0.005	0.007	0.03	0.01	0.1
D_{spl}	0.01	0.0001	0.0001	0.001	0.0005	0	0	0	0	0	0	0	0.15
D_{gnt}	5.5	0.0002	0.0007	0.001	0.0001	0.0001	0.0005	0.0005	0.07	0.0011	0.32	0.44	0.28

Element	Na	Y	Ga	Sc	V	Mn	Co	Cr	Ni
Prim. c_s (ppm)	2670	4.3	4	16.2	82	1045	105	2625	1960
Dep. c_s (ppm)	2151.4	4.07	3.2	16.3	79	1045	106	2500	1960
r_i (VIII) (Å)	1.18	1.019		0.87		0.96	0.9		
r_i (VI) (Å)	1.02	0.9	0.62	0.745	0.54	0.83	0.745	0.615	0.69
$v+$	1	3	3	3	5	2	2	3	2
D_{ol}	0.00001	0.005	0.04	0.16	0.06	0.5	1	0.3	9.4
D_{cpx}	0	0.2	0.74	0.51	1.31	0.44	2	3	9.4
D_{opx}	0.05	0.005	0.2	0.33	0.9	0.7	2	1.5	9.4
D_{spl}	0	0	5	0	0	0.25	2	300	0
D_{gnt}	0.04	2.11	5	2.27	1.57	2.05	2	5.5	0

Table S2. Mineral constants

Mineral	SiO_2	TiO_2	Al_2O_3	Cr_2O_3	FeO	MnO	MgO	CaO	Na_2O	K_2O
i_{mol}	60.09	79.90	102.0	151.99	71.85	70.94	40.30	56.08	61.98	94.20
C_i	1	1	2	2	1	1	1	1	2	2
O_i	2	2	3	3	1	1	1	1	1	1

Table S3. Results of mid-oceanic ridge models displayed in Figures 4, 6 and 7 of the main text. T_p = potential temperature; R_s = half spreading rate; sp-gnt = spinel-garnet transition zone depth; x_f = melt-focusing distance; T_c = crustal thickness. Prim. and Dep. indicate primitive and depleted mantle, respectively.

$\mathbf{T}_p$ (°C)	$\mathbf{R}_s$ (cm yr^{-1})	Source	sp-gnt (km)	$\mathbf{x}_f$ (km)	$\mathbf{T}_c$ (km)	Na (wt%)	10^4(Sm+Gd)/Ti
1548	2.1	Dep.	69–70	62.5	3.19	3.33	9.63
1598	2.1	Dep.	69–70	78	5.58	2.51	8.96
1648	2.1	Dep.	69–70	93	8.68	1.98	8.79
1698	2.1	Dep.	69–70	106	12.22	1.65	8.66
1748	2.1	Dep.	69–70	107	14.94	1.45	8.34
1598	0.5	Dep.	69–70	61	3.46	3.60	8.99
1598	5	Dep.	69–70	70	5.05	2.19	8.97
1598	10	Dep.	69–70	55	4.27	1.87	8.91
1598	2.1	Prim.	69–70	78	5.93	2.02	8.08
1598	2.1	Dep.	59–60	78	5.58	2.51	9.26
1598	2.1	Dep.	79–80	78	5.58	2.51	8.81